

SACLANT UNDERSEA RESEARCH CENTRE REPORT



DISTRIBUTION STATEMENT A
Approved for Public Release
Distribution Unlimited

BEST AVAILABLE COPY

20030822 201

SACLANTCEN SR-342

**Backscattering from bioturbated
sediments at very high frequency**

**E. Pouliquen, A. P. Lyons, N.
G. Pace, E. Michelozzi, L. Muzi**

The content of this document pertains
to work performed under Project 03-D of
the SACLANTCEN Programme of Work.
The document has been approved for
release by The Director, SACLANTCEN.



Jan L. Spoelstra
Director

SACLANTCEN SR-342

intentionally blank page

**Backscattering from bioturbated
sediments at very high frequency**

E. Pouliquen, A. P. Lyons, N. G. Pace,
E. Michelozzi, L. Muzi

Executive Summary:

The environment significantly affects minehunting system performance. This is especially true in difficult minehunting conditions to detect low contrast mines in cluttered environments. Inexact performance predictions result in poor evaluations of mine clearance which in turn lead to inaccurate assessments of remaining risk to follow-on forces in the channel or area. In this context, the present report provides a quantification and understanding of environmental phenomena critical to acoustic backscattering at minehunting frequency. The following study demonstrates the unambiguous importance of seabed interface roughness, internal bioturbation and upper sediment structure for object detection. In some cases (e.g. in the presence of strong seabed inhomogeneities), minehunting sonar detection performances are believed to be strongly reduced. In order to remedy to these environmental limitation, it is clear that minehunting operations need to quantitatively account for the environmental conditions and adapt to them in near real time. The development of minehunting systems having an adaptive behavior as a function of the environment (i.e. in term of frequency sweep, sensing geometry, multi aspect coverage, etc...) is currently the object of ongoing research at SACLANTCEN.

SACLANTCEN SR-342

intentionally blank page

Backscattering from bioturbated sediments at very high frequency

E. Pouliquen, A. P. Lyons, N. G. Pace,
E. Michelozzi, L. Muzi

Abstract:

Recent backscattering measurements made in the Gulf of La Spezia (Italy) using a sonar operating at 140 kHz combined with thorough seabed interface and volume ground truth illustrate the dominance of seabed volume scattering. Three-dimensional fluctuation statistics of density variability and vertical density gradients, both of which relate directly to the level of bioturbation (e.g. sea shell fragments, burrows, pockets of water) have been quantified using X-Ray computed tomography. Two-dimensional interface roughness spectra have also been determined using a digital stereo photogrammetry system. The combined ground truth has allowed a backscattering model to be fully constrained. Measured backscattering strength versus angle is compared to a model that includes the effects of varying density and sound speed. Data-model comparisons show that scattering from the volume of strongly inhomogeneous sediments can often be a primary contributor to seafloor scattering away from normal incidence.

Resumé:

De récentes mesures effectuées dans le Golfe de La Spezia (Italie) par un sonar opérant à une fréquence de 140 kHz combinées à une mesure approfondie des propriétés d'interface et de volume ont permis d'illustrer la dominance de la diffusion de volume. Des mesures tri-dimensionnelles des fluctuations statistiques de la variation de la densité ainsi que des mesures de gradients verticaux (ces phénomènes étant tous deux liés à la présence de fragments de coquilles, de terriers et de poches d'eau) ont permis de quantifier de nombreux paramètres de volume grâce à une technique de tomographie utilisant des rayons X. La rugosité bi-dimensionnelle d'interface a été déterminée grâce à un système stéréo-photogrammétrique numérique. La combinaison de ces deux mesures in-situ a permis de fournir tous les paramètres nécessaires à un modèle simple de rétrodiffusion. Les mesures angulaires de section efficace de rétrodiffusion sont comparées au modèle incluant les effets de variation de densité et de célérité. La comparaison modèle-données montre que la diffusion de volume de sédiments très inhomogènes peut très souvent être le premier contributeur à la diffusion totale, principalement aux incidences non verticales.

Keywords: high-frequency acoustics, acoustic scattering, seafloor scattering.

Contents

1	Introduction	1
2	Model description	3
2.1	Interface scattering	3
2.2	Volume scattering	5
2.3	Effect of vertical gradients	6
3	Seabed geo-acoustic properties	8
3.1	Core data description	8
3.2	Density gradient estimation	16
3.3	Interface roughness characterization	16
3.4	Seabed geo-acoustic properties summary	18
4	Model-Data comparison	29
4.1	Effect of the gradient on the reflection coefficient	29
4.2	Tellaro	29
4.3	Venere Azzura	30
4.4	Porto Venere	30
4.5	Punta della Mariella	30
5	Summary	37
	References	40

1

Introduction

The increasing use of sonars and echosounders at very high frequencies (i.e. $f \geq 100$ kHz) for bathymetry, seabed characterization and object detection relies on the assumption that scattering from the seabed is essentially caused by the rough water-sediment interface and its impedance contrast. This assumption is mainly motivated by the (apparently) prohibitive high attenuation of the compressional wave within the sediment volume. However, very high frequency measurements of seabed backscattering strength have not been able to validate this hypothesis and prove an unambiguous dominance of interface scattering. In contrast to measurements below 100 kHz that impute scattering from the seabed to both interface and volume scattering, [1]-[10], very little knowledge is available above 100 kHz. Stanic [10] presented backscattering data above 100kHz from which it was impossible to identify either a clear angular or frequency dependence, or the physical causes of the measured backscattering levels.

Until recently, modeling and validated measurements at these very high frequencies have been limited by the difficulty of accurately characterizing seabed properties at centimeter and sub-centimeter scales. Both interface roughness and the internal structure of the first tens of centimeters of the seabed require accurate measurement tools that are non-destructive and that have high spatial resolution. These tools, such as underwater two-dimensional digital photogrammetry [11] and three-dimensional X-Ray computed tomography [12] [13], have only become recently available. In addition to classical techniques (e.g. core velocity profiling and grain size analysis), these new techniques allow quantification of interface roughness spectra as well as millimeter scale resolution measurement of the internal sediment density structure. These parameters are direct inputs to acoustic scattering models and enable their validation.

Physics-based models designed for applications below 100 kHz have not yet been validated at higher frequencies. The so-called Lambert's law is still the most commonly used approach to empirically predict backscattering from the seabed above 100 kHz [14]. This law implicitly assumes that the seafloor is a perfectly diffuse reflector in the upper space. This simple approach reduces the effect of many possible seabed scattering mechanisms to a single and often physically ambiguous value. For example, what appears to be acoustically bright on sidescan sonar images could be caused by a seafloor with a smooth interface and inhomogeneous sub-structure in-

stead of the expected rough and hard surface. With the advent of new tools capable of finely characterizing the seabed on a sub-centimeter scale, it now seems natural to treat above 100 kHz both interface and volume scattering mechanisms (instead of simply treating seabed scattering as a Lambertian process) as each may be caused by different and sometimes independent seabed physical processes.

Vertical velocity, density and attenuation gradients observable in the first few centimeters of unconsolidated sediments have the potential to particularly affect high frequency scattering. In shallow water where bioturbation in sediments is often present, these gradients often exist over vertical distances larger than the incident acoustic wavelengths, significantly modifying the local water-sediment impedance contrast and related acoustic properties. As a consequence, the concept of a reflection and transmission coefficient between two homogeneous media both having constant average geo-acoustic properties may not be appropriate at very high frequency. As will be detailed further, the presence of property gradients often reduces interface backscattering levels while strongly augmenting the relative proportion of volume backscattering to total backscattering.

Although it seems a priori counter intuitive, the present study will show that, at very high frequency, volume scattering from the thin upper layer of unconsolidated soft and inhomogeneous sediments may be the dominant component of bottom backscattering, especially in the mid-angle range where dominance of volume scattering has often been observed below 100 kHz. The present work also demonstrates the importance of the effect of upper sediment gradients on very high frequency seabed backscattering. The next section describes the backscattering models used to account for gradient effects, interface and volume backscattering. Section 3 presents the fine scale geoacoustic characterization of four sites in the Gulf of La Spezia (Italy) where density gradients and density fluctuations were observed and quantified. In section 4, a comparison between the measured and predicted backscattering strength (BS) at these four sites is made. Section 5 presents a summary and a discussion on the obtained results.

2

Model description

To predict the relative proportion of sediment volume backscattering against interface backscattering above 100 kHz, several approaches are available. Classical approaches like the ones presented by Jackson [15] and Yamamoto [16] have been retained in this work mainly for the sake of simplicity. These relatively simple models have been validated below 100 kHz and are based on the tangent plane approximation (TPA) and on the small perturbation theory (PT) to treat backscattering from the water-sediment interface[15] and on the small perturbation model to predict volume backscattering [16]- [19]. The TPA is an intuitive high frequency approximation derived from physical optics. It becomes inaccurate when shadowing occurs (i.e typically when the grazing angle becomes small). Regarding the perturbation theory as applied to interface scattering, it can be seen as a lower frequency, low grazing angle approach. The conditions for which each of these theories break down for pressure release surfaces are discussed in detail in [20] [21] for Gaussian roughness spectra.

2.1 *Interface scattering*

The backscattering strength is assumed to be the incoherent sum of the interface and volume backscattering strengths. Each interface and volume component is therefore treated separately. It is also assumed that the coherent component of the backscattered field is zero.

2.1.1 *Tangent plane approximation*

To model the interface backscattering cross section for the case of no gradient, we use the classical tangent plane approximation (or Kirchhoff approximation). Following Jackson [15] but using the reflection coefficient evaluated at the grazing angle rather than at normal incidence, the TPA yields for the interface scattering cross section:

$$\sigma_s(\theta) = \left(\frac{k_a R_{12}(\theta)}{2\pi \sin(\theta)} \right)^2 \int_{-\infty}^{+\infty} \int_{-\infty}^{+\infty} \exp[2ik_a \cos(\theta)x - 2k_a^2 \sin^2(\theta)D(\mathbf{r})] d^2\mathbf{r}, \quad (1)$$

where k_a is the wavenumber in the water, θ is the grazing angle, and $R_{12}(\theta)$ is the plane wave reflection coefficient between the water of impedance $\rho_w c_w$ and the sediment of impedance $\rho_s c_s$ (in the case of no gradient). In this study, for the sake of simplicity, we assume an isotropic power-law spectrum for roughness of the following form:

$$W(\mathbf{k}) = \beta k^{-\gamma}. \quad (2)$$

As described in greater detail in [15], the structure function D present in Eq. 1 and the roughness power spectrum are connected by the following transformation:

$$D(\mathbf{r}) = 2 \int_{-\infty}^{+\infty} \int_{-\infty}^{+\infty} (1 - \cos(\mathbf{k} \cdot \mathbf{r})) W(\mathbf{k}) d^2 k. \quad (3)$$

In the case of the power law spectrum of Eq. 2, the structure function takes the simple form:

$$D(\mathbf{r}) = C_h^2 r^{\gamma-2}, \quad (4)$$

with

$$C_h^2 = [2\pi\beta\Gamma(3 - \gamma/2)2^{-(\gamma-2)}]/[(\gamma/2 - 1)(2 - \gamma/2)\Gamma(\gamma/2)]. \quad (5)$$

The technique used to characterize the roughness power spectrum and obtain values for β and γ is described in section 3.3.

2.1.2 Perturbation theory

When the small scale RMS relief is much smaller than the acoustic wavelength, the Rayleigh-Rice perturbation approximation (or simply the perturbation approximation) can be applied to the small scale portion of the water-sediment interface [22]. In this paper, the backscattering strength using the first order perturbation theory also follows Jackson's formulation for a penetrable two-fluid interface [15] and is expressed as

$$\sigma_s(\theta) = 4k_a^4 \sin^4(\theta) F(\theta, \nu, m) W(2k_a \cos(\theta)), \quad (6)$$

with,

$$F(\theta, \nu, m) = \begin{cases} \frac{[(m-1)^2 \cos^2(\theta) + m^2 - \nu^2]^2}{[m \sin(\theta) + (\nu^2 - \cos^2(\theta))^{1/2}]^4} & \theta > \theta_c \\ \frac{[(m-1)^2 \cos^2(\theta) + m^2 - \nu^2]^2}{[(1-m^2) \cos^2(\theta) + m^2 - \nu^2]^2} & \theta < \theta_c. \end{cases} \quad (7)$$

The parameter m in this equation is the sediment-water density ratio ($m = \rho_s / \rho_w$), ν is the velocity ratio ($\nu = c_s / c_w$) and θ_c the critical angle. The expression σ_s in Eq. 6 is also referred to as the small scale backscattering cross section. Assuming that the slope of the large-scale surface is a Gaussian-distributed random variable, Jackson averages this cross section to account for shadowing [15]. This assumes a cutoff wavenumber in the roughness spectrum that is somewhat arbitrary but that has the merit of providing a solution that accounts for the shadowing effect. Following Eqs. 19-24 from [15], one obtains a low grazing angle solution to the backscattering cross section, setting the RMS slope of the large-scale surface arbitrarily to 0.08 radian.

2.2 Volume scattering

To treat scattering from sediment density and velocity fluctuations, the expression for the volume backscattering strength (i.e. the differential backscattering cross section per unit surface) is taken from Yamamoto [16]:

$$\sigma_a(\theta) = \sigma_v \frac{\cos(\theta')}{4\alpha} T_{12}^2 T_{21}^2 \left\{ \frac{\sin^2(\theta')}{\sin^2(\theta)} \frac{\cos^2(\theta)}{\cos^2(\theta')} \right\} \quad (8)$$

The quantity α stands for the sediment compressional attenuation, T_{12} is the water-sediment transmission coefficient, T_{21} is the sediment-water transmission coefficient, θ is the incident angle, θ' is the refracted grazing angle. This expression is obtained for a smooth water-sediment interface. Ideally, the scattering effect at the crossing of the rough interface should be taken into account as is done by Ivakin [19] but for smooth surfaces, it has a negligible effect on the resulting volume backscattering strength. The scattered differential cross section per unit volume σ_v is obtained from Chernov [17] and is based on the first order perturbation theory. With the assumption that relative density variations and relative velocity variations are correlated accordingly,

$$\frac{\delta c}{c_s} = \eta \frac{\delta \rho}{\rho_s}, \quad (9)$$

the local volume backscattering cross section σ_v can be expressed as

$$\sigma_v(\theta) = 2\pi k_a^4 (1 + \eta)^2 S_\rho(2k_a), \quad (10)$$

where $S_\rho(2k_a)$ is the three-dimensional (3-D) power spectrum of the relative density fluctuations evaluated at the Bragg wavenumber, as was done for interface scattering. The value of $S_\rho(2k_a)$ is estimated from X-Ray computed tomography scans as described below. Also, as only density fluctuation measurements are available, the value of η needs to be fixed arbitrarily. It is fixed to 1/3 in accordance with average values measured by Yamamoto [16] [23] for unconsolidated sediments.

2.3 Effect of vertical gradients

As the acoustic frequency increases (and wavelength decreases), it is no longer possible to consider the area between water and sediment as a well-marked interface between two media. At very high frequency, vertical gradients may be of larger scales than the actual acoustic wavelength and may significantly affect reflection and transmission from and through such a medium. Here, the effect of gradient is considered as only affecting the reflection and transmission coefficient. In the presence of gradient, an effective reflection coefficient R_{12}^{eff} is substituted to R_{12} in Eq.1. The effective transmission coefficients T_{12}^{eff} and T_{21}^{eff} replace T_{12} and T_{21} respectively in Eq.8. In Eq.7, the density ratio m and velocity ratios are replaced by effective ratios, m_{eff} and ν_{eff} respectively.

There are several approaches for computing R_{12}^{eff} , T_{12}^{eff} and T_{21}^{eff} . This can be done following Brekhovskikh's approximation of the reflection coefficient for a gradient described by an arbitrary law [6] and the particular case of a density profile of the following form (see Lyons [25]):

$$\rho(z) = \rho_w \quad \text{if } z < 0 \quad (11)$$

$$\rho(z) = \rho_s - \frac{\rho_s - \rho_0}{1 + az} \quad \text{if } z \geq 0 \quad (12)$$

However, in the presence of both density and velocity gradients, a numerical computation is at present the only tractable way to obtain these coefficients. In the present case, velocity is assumed to behave like density (ρ in Eq.12 is replaced by c). The OASES reflection coefficient module (OASR [26]) is used to compute the plane wave coefficients. It should be noted that, in the case of gradient, the scattering cross section obtained with the TPA and that obtained with small perturbation theory are expected to differ because of a difference in computing R_{12}^{eff} and the term

$F(\theta, \nu_{eff}, m_{eff})$ in Eq. 7. In the former case, R_{12}^{eff} is obtained from OASR and in the latter $F(\theta, \nu_{eff}, m_{eff})$ is obtained using $m_{eff} = \rho_0/\rho_w$ and $\nu_{eff} = c_0/c_w$. The following section illustrates the effect of gradient on the reflection coefficient for the considered study sites.

3

Seabed geo-acoustic properties

Four sites in the Gulf of La Spezia (Italy) have been considered in this study: Tellaro (TE), Venere Azzura (VA), Porto Venere (PV) and Punta della Mariella (PdM). The sites have a water depth which varies from about 10 to 20 m. For each of the sites, diver cores and stereo-photographs were obtained. At two of the locations, PV and PdM, visibility was too poor to obtain good quality stereo-images of the seabed interface. The stereo photographs were further processed to obtain two-dimensional height fields and the cores were X-ray CT scanned (Fig. 1)).

3.1 Core data description

The four samples that were collected have lower average grain size than those presented in[13], ranging from very fine sand to silty-clay. The grain size analysis presented in Table 1 reveals for each of them very different combinations of sand, silt and clay. To reduce disturbance, the cores were taken manually by divers. All were taken with the longitudinal axis of the core liner kept horizontal (hereafter referenced as the Z-axis). This uncommon geometry was justified by the difficulty of scanning a vertical core. Since the internal diameter of the gantry around which X-Ray emitters and detectors rotate is fixed, a vertical core with the requirement that its original in situ orientation be kept would have had to be short enough to pass through. As this study concerns very high frequency volume scattering (i.e. typically above 100 kHz, corresponding to centimetric to sub-centimetric acoustic wavelengths), a core diameter of 10 cm was found to be sufficient to capture sediments over several wavelengths in the vertical direction (i.e. the Y-axis). The horizontal sampling also enabled an analysis of the horizontal stationarity of density properties.

X-ray CT scans were performed within hours after in-situ sampling to reduce compaction and decomposition. Although the cores were kept unopened during the entire procedure there exists the possibility that some of the cores may not have remained at ambient pressure until the CT scans took place. The cores were scanned using a Picker PQ2000S scanner. Voxel dimension varied between cores as described in Table 2.

Although different types of interaction are possible, the relatively low energy of

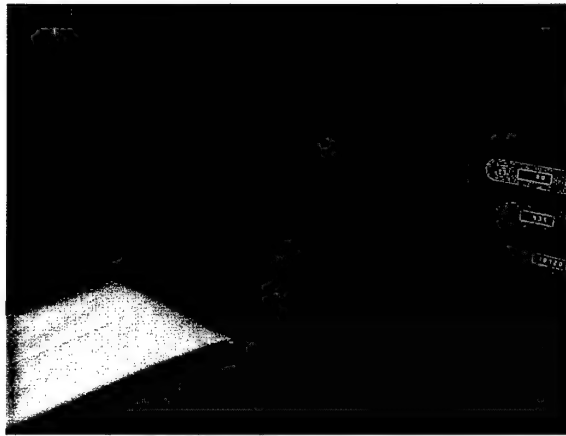


Figure 1 Illustration of the procedure employed to perform X-Ray tomography on the horizontal cores.

Table 1 Grain size properties at the four study sites

	Water depth (m)	Sand/Silt/Clay %/%/%	Mean grain diameter (mm)
TE	14.2	75/15/10	0.0507
VA	9.8	20/70/10	0.0145
PV	12.3	00/40/60	0.0018
PdM	21.5	15/50/35	0.0068

X-rays used by CT scanning reduces the number of relevant phenomena to photoelectric effect and Compton scattering. It has been determined that for seafloor sediments, there is a linear dependence between bulk density and CT scan numbers (in Hounsfield units) [12]. The calibration approach discussed in [12] is used to determine the relationship between Hounsfield units and bulk density.

Subsequent data processing similar to that described by Tang [13] was carried out to obtain estimates of power spectra. As described in detail in [13], the three-dimensional density power spectrum is effectively computed as follows:

$$\begin{aligned}
 S_{u,v,w} &= \frac{\Delta x \Delta y \Delta z}{(2\pi)^3 N_x N_y N_z} & (13) \\
 &\times \left\langle \left| \sum_{l,m,n=0}^{N_x-1, N_y-1, N_z-1} H_{l,m,n} \cdot \frac{\rho(l, m, n) - \bar{\rho}}{\bar{\rho}} \right|^2 \right\rangle
 \end{aligned}$$

Table 2 *Geometrical properties of each X-ray CT data set.*

	Voxel size (mm ³) (mm ³) $\Delta x \times \Delta y \times \Delta z$	Slice pixel number $N_x \times N_y$	Number of slices N_z
TE	.35 x .35 x 2	290 x 290	293
VA	.25 x .25 x 2	318 x 318	137
PV	.35 x .35 x 2	318 x 318	119
PdM	.25 x .25 x 2	400 x 400	183

$$e^{-i2\pi[lu/N_x + mv/N_y + nw/N_z]/2} \rangle$$

The term $\bar{\rho}$ is the average density within the core sample, away from the edges where compaction may occur. A three dimensional window function $H_{l,m,n}$ is used to reduce leakage in the spectrum estimation. As in Tang [13], we use a three dimensional Hanning function $H(P)$.

$$H(P) = 1 - ((\mu - 1) \cos(\pi P) + \mu) \quad (14)$$

where P is a scaled radius which does not exceed unity.

$$P^2 = \left(\frac{x - L_x/2}{L_x/2}\right)^2 + \left(\frac{y - L_y/2}{L_y/2}\right)^2 + \left(\frac{z - L_z/2}{L_z/2}\right)^2 \quad (15)$$

The term μ is fixed to 0.5, H takes the form:

$$H(P) = \frac{1}{2}(1 + \cos(\pi P)) \quad (16)$$

The window function is normalized such that

$$\frac{1}{L_x L_y L_z} \int \int \int H^2(x, y, z) dx dy dz = 1. \quad (17)$$

The description of the internal structure of sediments using data derived from X-ray CT techniques has been the object of recent studies (mainly by Orsi[12] and more recently by [13]). In [13], the analysis of the density spectra of sandy sediments showed three types of variability: the intrinsic variability of the sand matrix, shells

and mud mixtures. The three dimensional power spectra of density fluctuation were well modeled by a two component power law, and in contrast to previous assumptions, an exponential correlation function was found not to be suitable for these sediments. Even though these conclusions might be valid for some sandy sediments, a number of questions still remain open. Despite the apparent isotropic nature of the sediments studied by Tang [13], organized distributions of individual scatters (shells or mud intrusion) or the presence of layering can often be observed. Their effects on acoustic scattering are not yet understood. While modified power law spectra are possibly suitable for sandy sediments, it is still of interest to determine whether or not this spectral description is also suitable for other sediment types especially to those with finer grain sizes which are more likely to be affected by a strong heterogeneity and/or bioturbation.

There is a limitation in using a single core sample to characterize the spectral nature of highly bioturbated sediments, as is the case in this study. Even though low spatial frequencies are represented in one core, information from a single data set may not be sufficient to obtain a well-determined average power spectrum. In other words, the lower the spatial frequency, the smaller the relative statistical population and therefore, the less well defined the average power spectrum for larger-scale fluctuations. To ensure proper ensemble averages, larger data sets in size and number from a statistically homogeneous region are required but are not available in the present study. Also, the Gaussian nature of the density distribution may be questioned as mud intrusion and shell pieces may not be considered as a simple additive process to the intrinsic mixture of mineral grains and water.

In the presence of a three-dimensional isotropy of the density field, the spectrum S_ρ can be radially averaged to obtain a smoother spectrum \bar{S}_ρ . By switching to spherical coordinates, the spectrum \bar{S}_ρ averaged over a wavenumber width of Δk is obtained as follows:

$$\begin{aligned}\bar{S}_\rho(k) &= \frac{1}{4\pi \int_k^{k+\Delta k} k^2 dk} \\ &\times \int_{\psi=0}^{2\pi} \int_{\phi=-\pi/2}^{\pi/2} \int_k^{k+\Delta k} S_\rho(k, \phi, \psi) k^2 dk \cos(\phi) d\phi d\psi\end{aligned}\quad (18)$$

The one-dimensional density power spectra S_u , S_v , S_w , respectively in the X, Y and Z direction are computed by double integration of the three dimensional density power spectrum $S_{u,v,w}$:

$$S_u = \Delta k_y \Delta k_z \sum_{m,n=0}^{N_y-1, N_z-1} S_{u,v,w} \quad (19)$$

$$S_v = \Delta k_x \Delta k_z \sum_{l,n=0}^{N_x-1, N_z-1} S_{u,v,w} \quad (20)$$

$$S_w = \Delta k_x \Delta k_y \sum_{l,m=0}^{N_x-1, N_y-1} S_{u,v,w} \quad (21)$$

For each core, three one-dimensional spectra and a radially averaged spectrum are computed. The results are given in the following subsections and compiled in Table 3.

3.1.1 Tellaro

Sediments at this site are silty-sands with only few small shell fragments. The slice of the two dimensional spectrum at $k_z = 0$ (Fig. 2) shows an anisotropy. This deviation can be due to an error of the estimation of the vertical axis or compaction during the coring process. Anisotropy is not observed in the two other planes. Away from the lower spatial frequency region of the spectrum which displays some fluctuation due to under-representation of the statistical population, the one-dimensional marginal spectra show only small discrepancies with each other at higher spatial frequencies (Fig. 3). The slope of the spectrum is steeper above $\log_{10}(k) = 3.5$ than the slopes observed by Tang for sandy sediments [13]. Figure 4 shows the behavior of the radially averaged three-dimensional spectrum. It clearly does not behave like a modified power law-term of the form:

$$S_{\rho|model-3D}(k) = \frac{l_1 \gamma_1}{\pi} \cdot \frac{a_1}{[1 + (l_1 k)^2]^{\gamma_1 + 1}} \quad (22)$$

Emphasis in the fitting process was made on the higher frequency part of the spectrum because the lower frequency part of it suffers from statistical under-representation. A two component modified power law, as suggested by Tang [13], does not give a significantly improved fit at the expense of adding three more parameters. The solid line in Fig. 4 is the best fit to the measured spectrum ($a_1 = 6.0 \times 10^{-7} m$, $l_1 = 2mm$ and $\gamma_1 = 2.2$) in a least square sense. For the same reasons, many other combinations of analytical forms do not give a better fit over the entire spectral band.

3.1.2 Venera Azzura

Sediments at Venera Azzura are sandy-silts, with the presence of shell pieces and some sand. There is no visible presence of anisotropy in any of the three planes of reference (Fig. 5). This is confirmed by the behavior of the individual one-dimensional

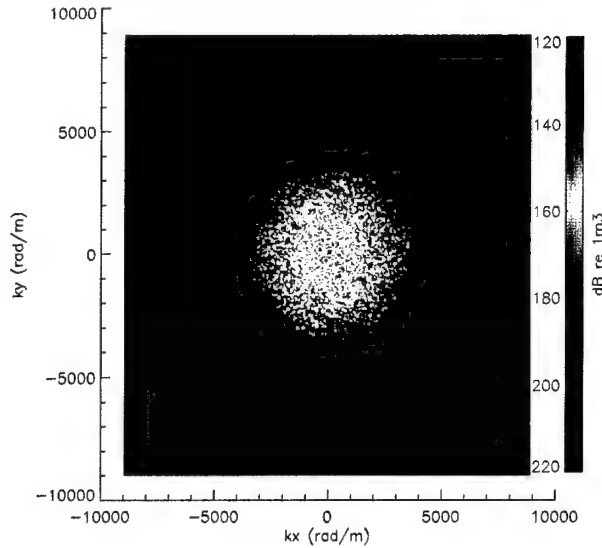


Figure 2 Slice of the three dimensional density power spectrum $S_\rho(k_x, k_y, k_z = 0)$ from the Tellaro dataset. Units are in dB re 1 m^3 .

spectra as displayed in Fig. 6. As for the Tellaro core analysis, a drop-off is also observable around $\log_{10}(k) = 3.5$. In the lower spatial frequency region, the slope of the power spectrum tends to zero.

In Fig. 7, the best fit obtained using the modified power law of Eq. 22 gives more satisfactory results than for Tellaro ($a_1 = 6.0 \times 10^{-7} \text{ m}$, $l_1 = 2 \text{ mm}$ and $\gamma_1 = 2.2$). The modified power law seems a good candidate to represent this sediment structure.

3.1.3 Porto Venere

Sediments at Porto Venere are clayey-silts with a strong presence of shell pieces, water pockets, worm burrows, and small stones. Figure 8 shows a false color three-dimensional reconstruction of the density field of the PV horizontal core. Although, the upper part of the core displays the water-sediment interface, the spectral analysis was performed excluding this region. This reconstruction illustrates the high spatial variability of density, both horizontally and vertically. Figure 9 is an artificial view of the internal structure of the density field made by removing the mid-density values and keeping visible the low and high density values (respectively the water pockets and the burrows in red and the shell pieces in yellow). This representation shows that 1) shell pieces are uniformly distributed in the core, 2) the low-density regions

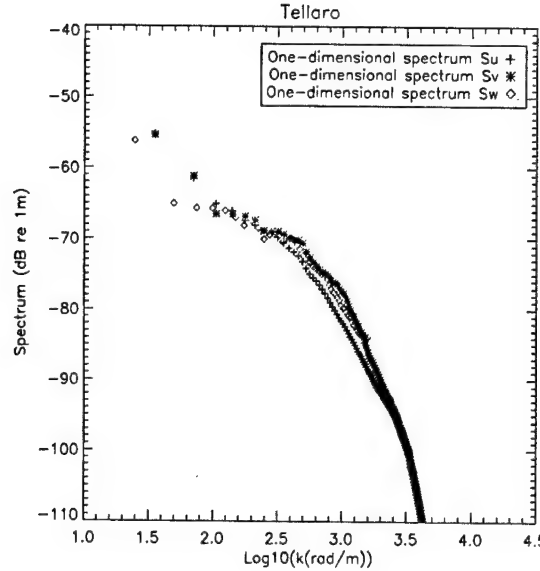


Figure 3 Three one-dimensional spectra S_u , S_v , S_w from the Tellaro dataset. Units are in dB re 1 m.

are not uniformly distributed over the sediment sample, 3) the shape and length of the low density regions (most likely burrows) are not completely random and tend to be oriented more vertically, and 4) the size of the low density regions is an order of magnitude larger than the size of the shell pieces.

The density power spectrum from this highly inhomogeneous medium is isotropic as can be seen in Fig. 10. In Fig. 11, the three one-dimensional power spectra overlay each other, except for the lowest spatial frequency region where the values become more random. The similarity of the one-dimensional spectra for the three orthogonal directions is strong evidence of isotropy, despite the presence of burrows that have an almost vertical orientation. A drop-off in the spectra is again observed around $\log_{10}(k) = 3.5$ but is less strong than for the two previous datasets. The radially averaged three-dimensional spectrum shown in Fig. 12 is well fit by a modified power law above $\log_{10}(k) = 2.3$. The model values are $a_1 = 6.0 \times 10^{-7} m$, $l_1 = 1.4 mm$ and $\gamma_1 = 2.8$. The dominance of the intrinsic density variations in the silty-clay sediment can explain this behavior in the high wavenumber portion of the spectrum. Below $\log_{10}(k) = 2.3$, the large-scale fluctuations caused by the burrows and shell pieces seem to be dominating the internal density structure. Curiously, oscillations of the PV spectrum in the low spatial frequency part do not seem to be larger in amplitude than those observed in the spectrum of TE where there is practically no large scale fluctuation (only a few small shell pieces and no significant burrows). One may therefore strongly question the cause of these oscillations of the spectrum

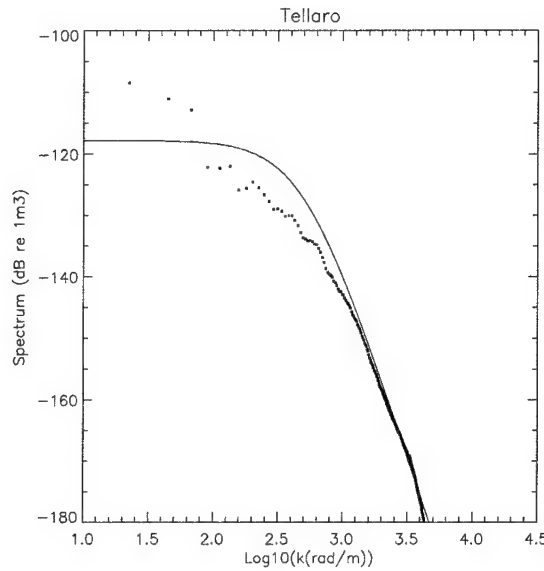


Figure 4 Radially averaged three dimensional spectrum \bar{S}_ρ from the Tellaro dataset (dots). The solid line corresponds to the best fit of the model. Units are in dB re $1 m^3$.

in the small wavenumber region. These oscillations may simply be due to the limits imposed by the actual physical size of the dataset.

3.1.4 Punta della Mariella

The sediments at Punta della Mariella are a mixture of clay and silt, with also a strong presence of shell pieces, water pockets and bioturbation. This is the most inhomogeneous site of the study. The density fluctuation spectrum of the core taken at this site shows near perfect isotropy. The one-dimensional spectra, taken along the three main axes, all behave identically as displayed in Fig. 13. A modified power law does not fit well the three-dimensional radially averaged spectrum in Fig. 14. The best model values are $a_1 = 1.0 \times 10^{-6} m$, $l_1 = 1.2 mm$ and $\gamma_1 = 3.0$. A mismatch between model and data can again be observed in the low wavenumber portion of the spectrum, as seen in the spectra of TE and PV.

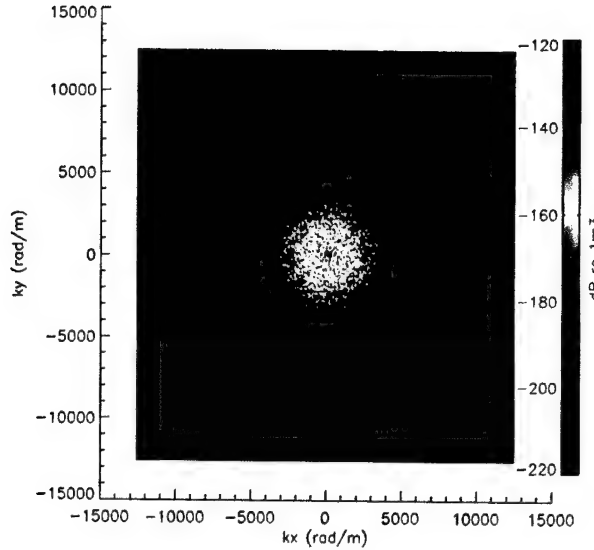


Figure 5 Slice of the three dimensional density power spectrum $S_\rho(k_x, k_y, k_z = 0)$ from the Venere Azzura dataset. Units are in dB re $1 m^3$.

3.2 Density gradient estimation

Computation of gradients is a difficult task because a) the X-Z plane of the core matrix is not perfectly horizontal and b) because of local roughness, all the individual profiles $\rho(l, 0 < m < N_y, n)$ for given combinations of l and n may not be systematically aligned with each other. Therefore, the first step in gradient computation consists in aligning all the vertical profiles $\rho(l, 0 < m < N_y, n)$ with each other. For each individual profile, the depth where the density crosses $1.1 g/cm^3$ is defined as being at a nominal 'altitude' of $-0.1 cm$. Once aligned, the second step consists in averaging the profiles as a function of depth. Figures 15, 16, 17 and 18 present the respective averaged profiles at the four considered sites. Each of them displays a distinct gradient pattern. The least pronounced gradient is at Tellaro, and the most pronounced one is at Punta della Mariella. The fit to the theoretical profile proposed in eq. 12 is done manually. Table 3 at the end of this section displays the chosen values of ρ_0 , ρ_s and a for each site.

3.3 Interface roughness characterization

Measurement of roughness power spectra W were obtained using a digital stereo photogrammetry system developed at SACLANTCEN. Providing visibility condi-

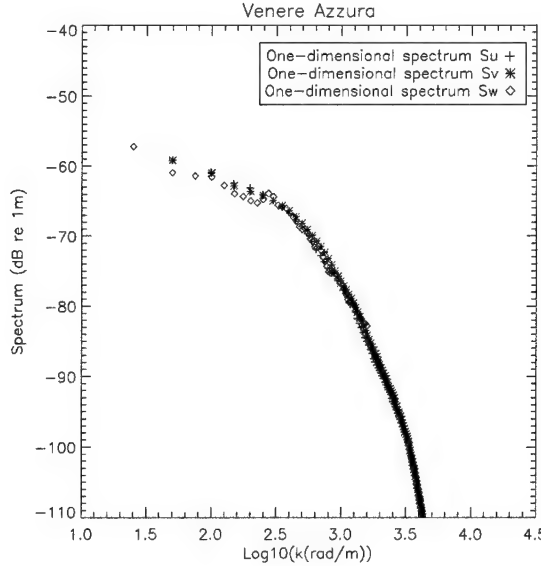


Figure 6 One-dimensional spectra S_u , S_v , S_w from the Venere Azzura dataset. Units are in dB re 1 m.

tions are good, the system gives a snapshot estimate of the two-dimensional water-sediment interface height field for a limited area (typically less than one square meter). The procedure employed to retrieve roughness spectra is described in detail in [11]. From the height field estimate, the roughness power spectrum can be computed (and subsequently values of β and γ can be estimated). Given the limited number of measurements per site, stationarity over a larger area is generally assumed. Visibility was sufficient only at TE and VA to retrieve roughness spectra with a good degree of confidence. At the two other sites PV and PdM, visibility was too poor to enable a satisfactory stereo reconstruction.

Figures 19 and 20 give a qualitative idea of interface roughness present at TE and VA respectively. One can notice the presence of burrow holes at VA and their absence at TE. There is a slight roughness anisotropy due to a light ripple field at TE but acoustic backscattering at this site did not show any significant difference between along and across the ripple crests. Figure 21 displays the retrieved height field at Venere Azzura. The magnitude of roughness at TE and VA is low, less than one centimeter RMS over the reconstructed height field. Assuming isotropy at both sites, β and γ , are estimated as defined by Eq. 2. It is made by performing a least square fit to the radially averaged roughness spectrum:

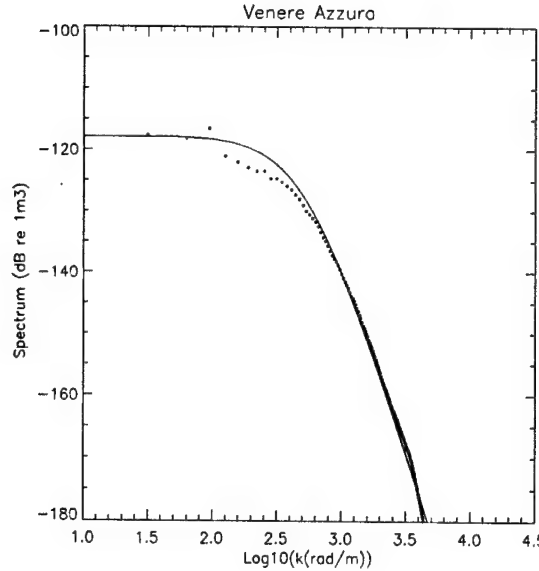


Figure 7 Radially averaged three dimensional spectrum \bar{S}_ρ from the Venere Azzura dataset (dots). The solid line corresponds to the best fit of the model. Units are in dB re $1 m^3$.

$$\bar{W}(k) = \frac{1}{2\pi \int_k^{k+\Delta k} k dk} \int_{\psi=0}^{2\pi} \int_k^{k+\Delta k} S_\rho(k, \psi) k dk d\psi. \quad (23)$$

Figures 22 and 23 show the roughness power spectra and their corresponding best fit using a power law spectrum. The fit is good above 0.06cycles/cm (i.e. for wavelengths smaller than approximately 20 cm).

3.4 Seabed geo-acoustic properties summary

By combining X-Ray CT scans, stereo photogrammetry techniques and grain size analysis, most geo-acoustic sediment properties needed for input to the model presented in section 2 have been characterized. They are compiled in Table 3. Parameters in parenthesis were those estimated without a dedicated measurement. Attenuation in particular was not measured but estimated from grain size measurements using Hamilton [27]. Because roughness estimates at PV and PdM were not available due to poor visibility conditions, β and γ were assumed identical to the values measured at VA. The value of $S_\rho(2k_a)$ is taken from the radially averaged spectra \bar{S}_ρ at the spatial frequency of interest ($2k_a = 1173 \text{ rad/m}$ at 140 kHz). This ensemble

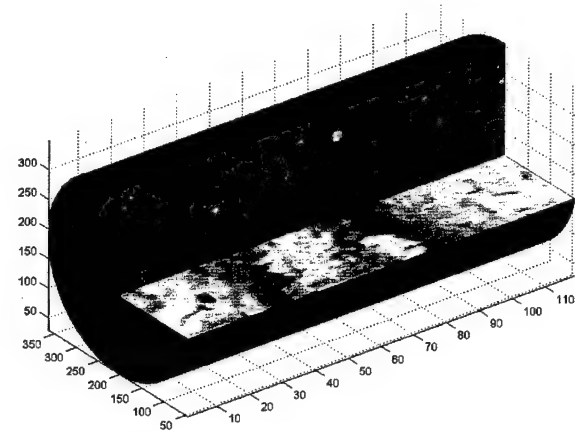


Figure 8 *False color 3-D reconstruction of horizontal core at PV; The size of the core is approximately $10 \times 10 \times 22 \text{ cm}^3$.*

of geo-acoustic properties enables the backscattering strength model presented in Section 2 to be almost fully constrained, requiring only a few of the parameters to be estimated.

BEST AVAILABLE COPY

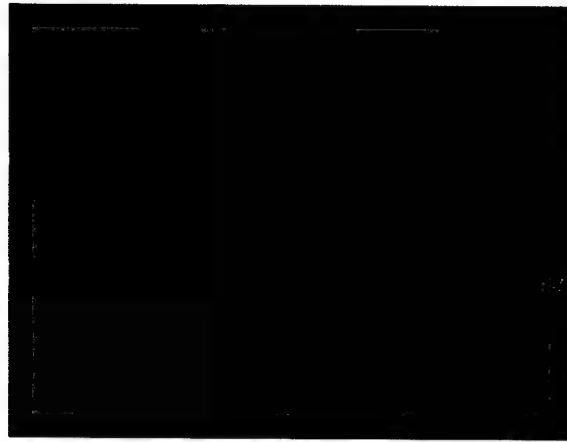


Figure 9 3-D visualization of burrows and water pockets (in red) and shell pieces (in yellow) in the horizontal core of Porto Venere

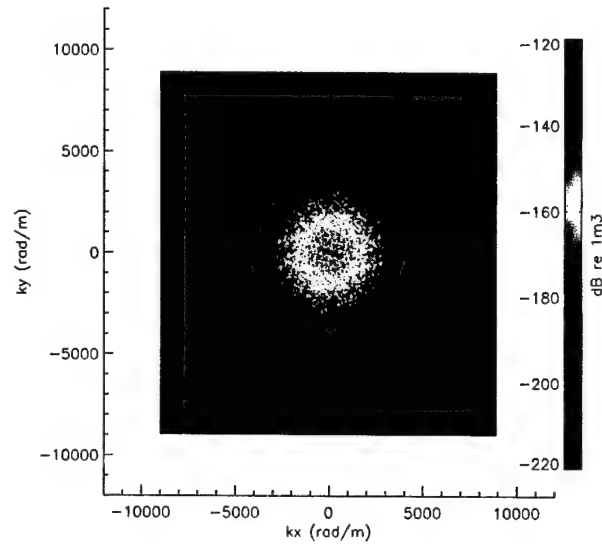


Figure 10 Slice of the three dimensional density power spectrum $S_\rho(k_x, k_y, k_z = 0)$ from the Porto Venere dataset. Units are in dB re 1 m^3 .

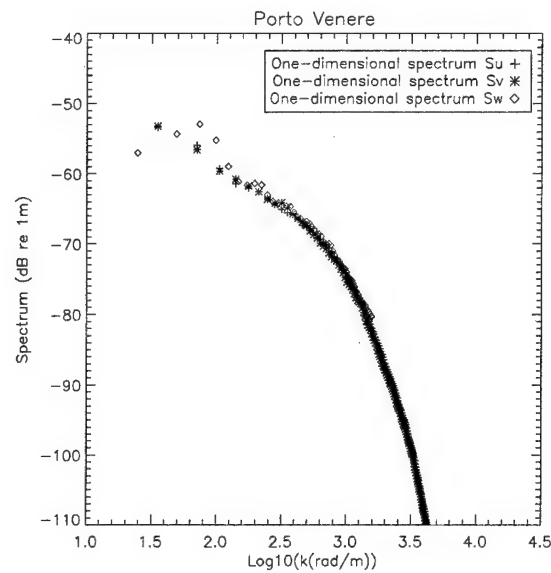


Figure 11 One dimensional spectra S_u , S_v , S_w of Porto Venere along the three axis. Units are in dB re 1 m.

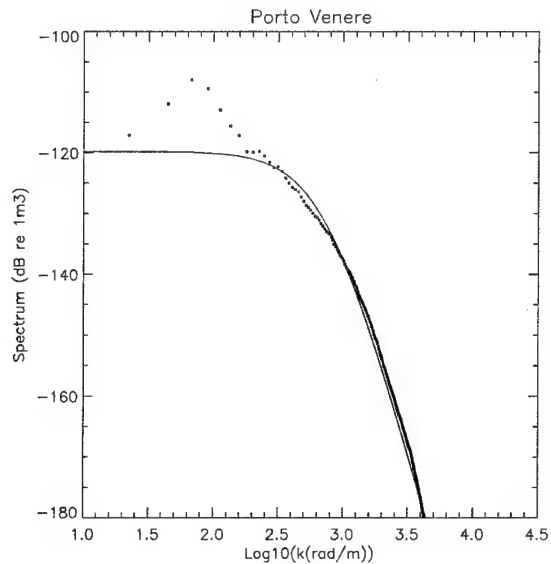


Figure 12 Radially averaged three dimensional spectrum \bar{S}_p from the Porto Venere dataset (dots). The solid line corresponds to the best fit of the model. Units are in dB re 1 m³.

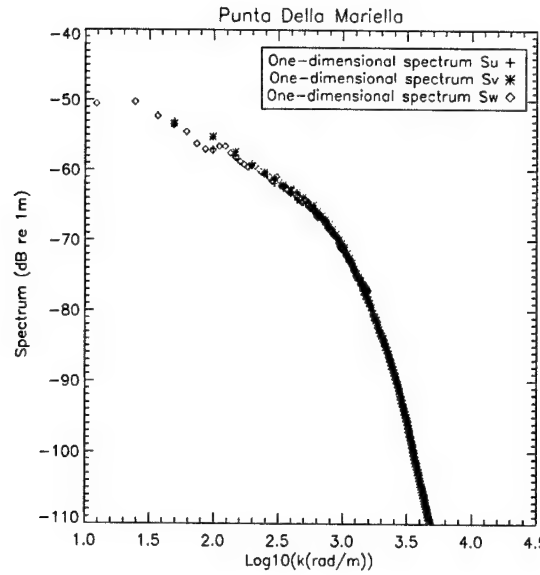


Figure 13 One dimensional spectra $W(k)$ of Punta della Mariella along the three axis. Units are in dB re 1 m

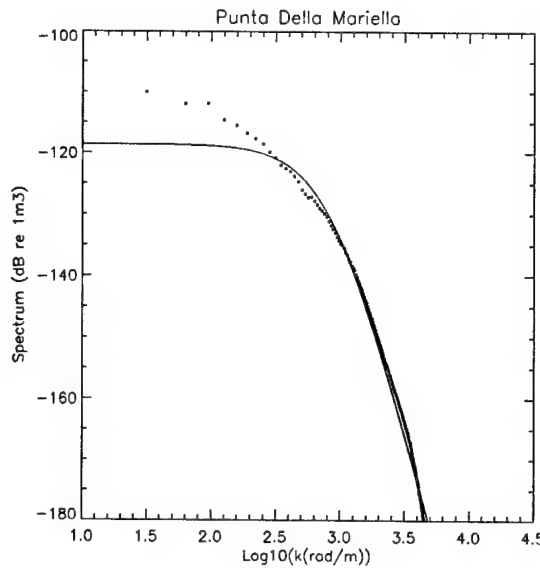


Figure 14 Radially averaged three dimensional spectrum \bar{S}_ρ of Punta della Mariella (dots). The solid line corresponds to the best fit of the model spectrum at high wavenumbers. Units are in dB re 1 m³.

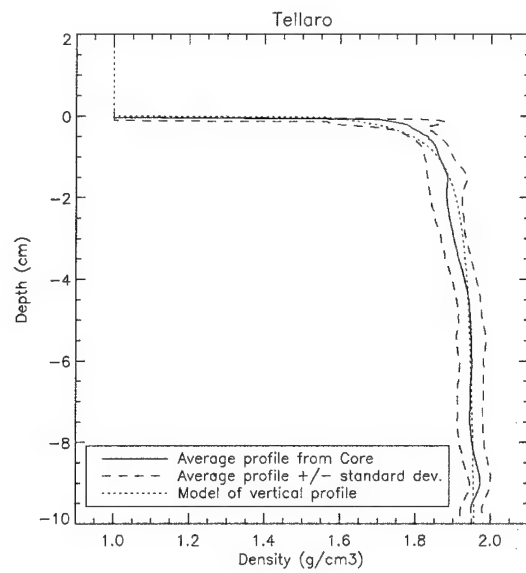


Figure 15 Average density profile, intervals of confidence and theoretical profile as a function of depth within the sediment of Tellaro

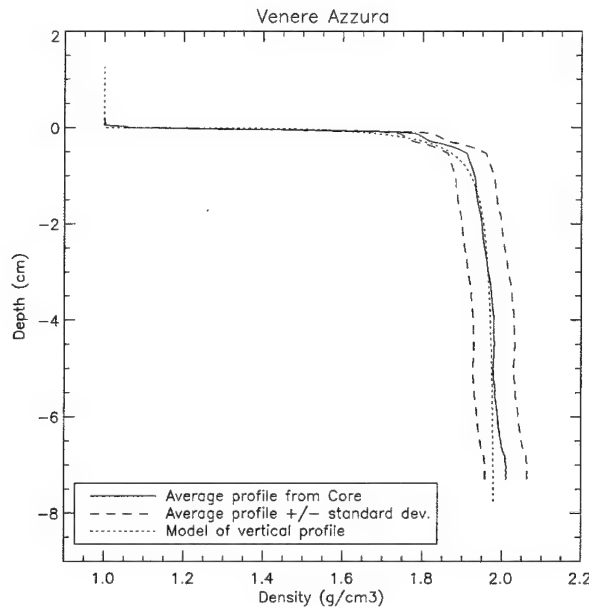


Figure 16 Average density profile, intervals of confidence and theoretical profile as a function of depth within the sediment of Venere Azzura

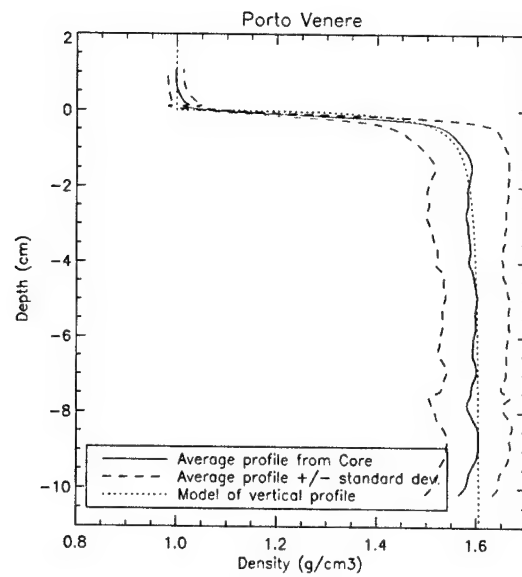


Figure 17 Average density profile, intervals of confidence and theoretical profile as a function of depth within the sediment of Porto Venere

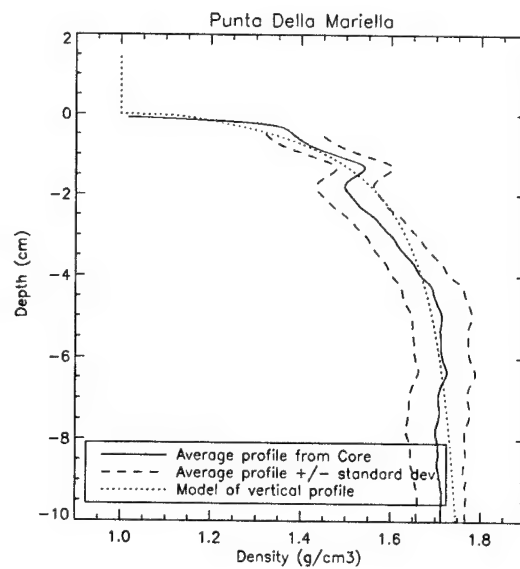


Figure 18 Average density profile, intervals of confidence and theoretical profile as a function of depth within the sediment of Punta della Mariella

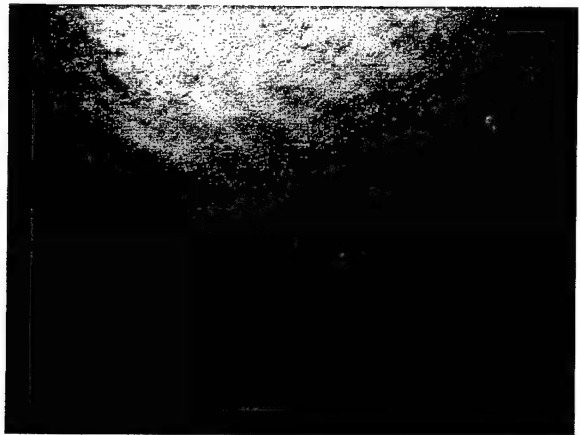


Figure 19 *Photography of the seabed interface at the Tellaro site.*



Figure 20 *Photography of the seabed interface at the Venere Azzura site.*

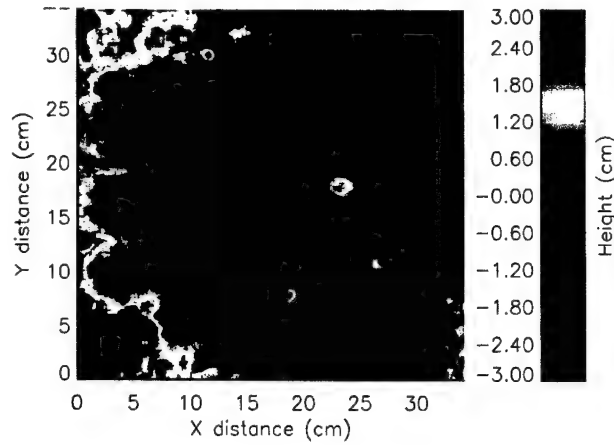


Figure 21 30 cm x 30 cm digital elevation model at Venere Azzura obtained using the stereo photo-grammetry technique.

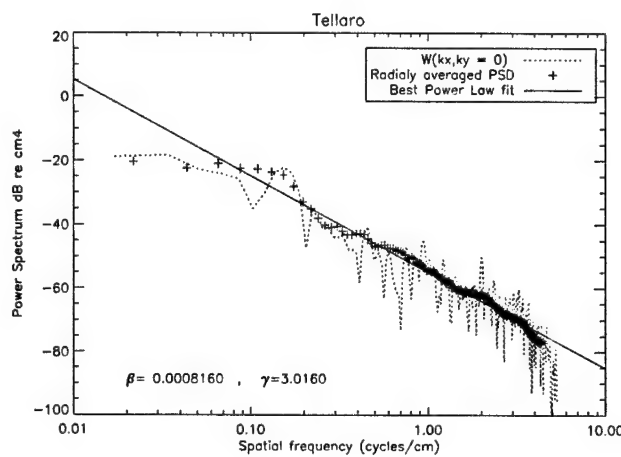


Figure 22 Roughness power spectrum at Tellaro. The solid line corresponds to the best fit with the radially averaged power spectrum \bar{W} . For comparison, the dashed line corresponds to the value of the 2-D roughness spectrum W at $k_y = 0$.

BEST AVAILABLE COPY

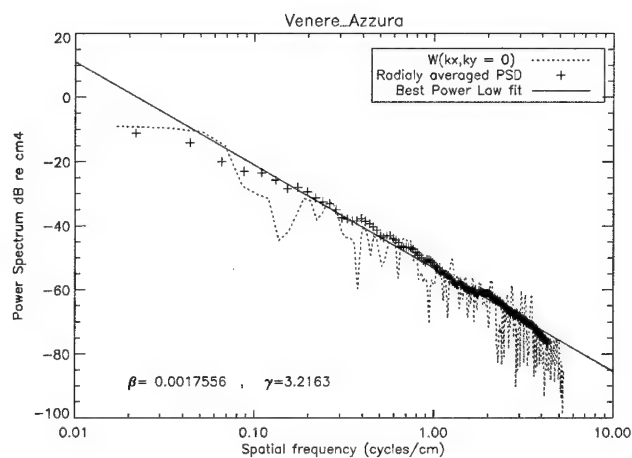


Figure 23 Roughness *poPouldu1* *wer* spectrum at Venere Azzura. The solid line corresponds to the best fit with the radially averaged power spectrum \bar{W} . For comparison, the dashed line corresponds to the value of the 2-D roughness spectrum W at $k_y = 0$.

Table 3 *Geoacoustic properties of the four study sites. Parameters in parenthesis are estimates.*

		TE	VA	PV	PdM
Volume Parameters					
Mean grain diameter	(mm)	0.0507	0.0145	0.0018	0.0068
Sand/Silt/Clay	%/%/%	75/15/10	20/70/10	00/40/60	15/50/35
Density Lab. Measurement ρ_s	(g/cm^3)	1.85	1.65	1.5	1.7
Density X-Ray Measurement ρ_s	(g/cm^3)	1.97	1.99	1.61	1.81
Compress. Attenuation α	($dB/m/kHz$)	(0.6)	(0.11)	(0.04)	(.10)
Sound speed c_s	(m/s)	1650	1520	1490	1530
$S_p(2k_a)$ @140kHz		-147.01	-144.7	-142.1	-138.5
Volume Scat. Strength σ_v	($dB rel m^{-3}$)	-25.80	-23.49	-20.89	-17.29
a_1	(m)	$6.0 \cdot 10^{-7}$	$6.0 \cdot 10^{-7}$	$6.0 \cdot 10^{-7}$	$1.0 \cdot 10^{-6}$
l_1	(mm)	2.0	2.0	1.4	1.2
γ_1		2.2	2.2	2.8	3.0
Roughness Parameters					
RMS roughness σ_h	(cm)	0.87	0.96	(0.96)	(0.96)
Spectral strength β	(cm^4)	0.00081	0.00175	(0.00175)	(0.00175)
Spectral exponent γ		3.02	3.21	(3.21)	(3.21)
Gradient Parameters					
Density ρ_0	(g/cm^3)	1.52	1.37	1.18	1.1
Sound speed c_0	(m/s)	1550	1510	1495	1515
a	(m^{-1})	300	800	800	100

4

Model-Data comparison

Acoustic data were acquired using a single element transmitter and a multi-element receiver mounted on a pan/tilt mechanism installed at the top of a telescopic tower. The source height above the seabed was approximately 4 m. An initial survey using a 300 kHz multibeam bathymetric echosounder ensured that the large scale slope was negligible. Sidescan sonar data and diver's observations confirmed the spatial stationarity of the superficial seabed properties over the acoustic footprints. Reception on the 64 element receive array enabled an angular beamforming. The backscattering strength as a function of grazing angle was computed by averaging independent beams over a receive sector width of 30°. Data displayed below are for a transmission of $50\mu\text{s}$ CW pulses with a center frequency of 140 kHz).

4.1 *Effect of the gradient on the reflection coefficient*

Figure 24 illustrates the effect of vertical gradients on the reflection coefficient at each of the four experiment sites. Near normal incidence, the effective reflection coefficient is lowered and approaches the reflection coefficient obtained for a sediment having an impedance of $\rho_0 c_0$ whereas at low grazing angle and particularly around the critical angle, the effective reflection coefficient gets closer to the reflection coefficient for an impedance of $\rho_s c_s$.

4.2 *Tellaro*

At Tellaro, as shown in Fig. 25, for the case of no gradient, modeled interface backscattering strengths and volume backscattering strengths are respectively too high and too low compared to the measured backscattering strengths. On the contrary, in the presence of property gradients, as the reflection coefficient is lowered by about 3dB, the modeled interface backscattering strength matches the data well. However, scattering within the volume is clearly not a competing mechanism at this site and at this frequency. This can be explained by the low amount of scatters within the volume and by a relative higher impedance contrast compared to the other sediments studied in this paper.

4.3 Venere Azzura

At Venere Azzura, interface and volume scattering have comparable levels (see Fig. 26). In the absence of gradients, interface scattering dominates at all grazing angles and is slightly higher than the measured level. The sum of interface and volume scattering overestimates backscattering. However, if vertical gradients are taken into account, interface scattering is reduced by about 3dB. The sum of interface and volume scattering matches almost exactly the measured backscattering strengths. In the low grazing angle portion, the measured backscattering strength decreases rapidly as the grazing angle decreases. This effect is not observable in the model even though self-shadowing is taken into account. One may actually question the physical processes responsible for the decay of backscattering strength at low grazing angle as well as accuracy of the simple model considered here. Clearly, self-shadowing is partly responsible for this decay even though roughness is often low for fine sediments, but it does not seem to be the only cause. As a suggested competing mechanism, the spatial fluctuation of sound speed at the sediment interface could also be responsible for this rapid decay, especially for highly inhomogeneous sediments. The presence of a distribution of sound speeds affects local refraction, reflection and transmission with a subsequent impact on the backscattering strength. The effect of local interface sound speed fluctuation is not treated here but should be the object of further investigations.

4.4 Porto Venere

Backscattering at Porto Venere is high and higher than at TE and VA, despite a similar low roughness and a lower water-sediment impedance contrast. This level can only be explained by the higher velocity and density fluctuation within the volume. As can be seen in Fig. 27, volume scattering dominates at moderate and low grazing angles both in the presence and in the absence of gradients. Given the low water-sediment density contrast the effect of the vertical gradient is even more significant in reducing the relative interface scattering. In the presence of property gradients, volume scattering is unambiguously the only significant scattering mechanism.

4.5 Punta della Mariella

The physical mechanisms responsible for scattering at Punta della Mariella are the same as at PV: sediments are strongly inhomogeneous and have a low impedance. In the absence of gradients, the sum of interface and volume backscattering strengths over predicts the measured levels. However, with a gradient, interface scattering is reduced and volume scattering alone is very close to the data. The slight overpredic-

tion of volume scattering alone may be due to an inaccurate estimation of some of the volume geoacoustic properties (gradient, inhomogeneity levels, degree of correlation between density and velocity fluctuation). Internal seabed properties are retrieved from a small volume ($10 \times 10 \times 36 \text{ cm}^3$ at PdM) which is assumed (possibly in error) representative of the properties of the entire acoustic footprint. However, general agreement between the model including gradients and the acoustic backscatter data is excellent and consistent for the 4 sites considered.

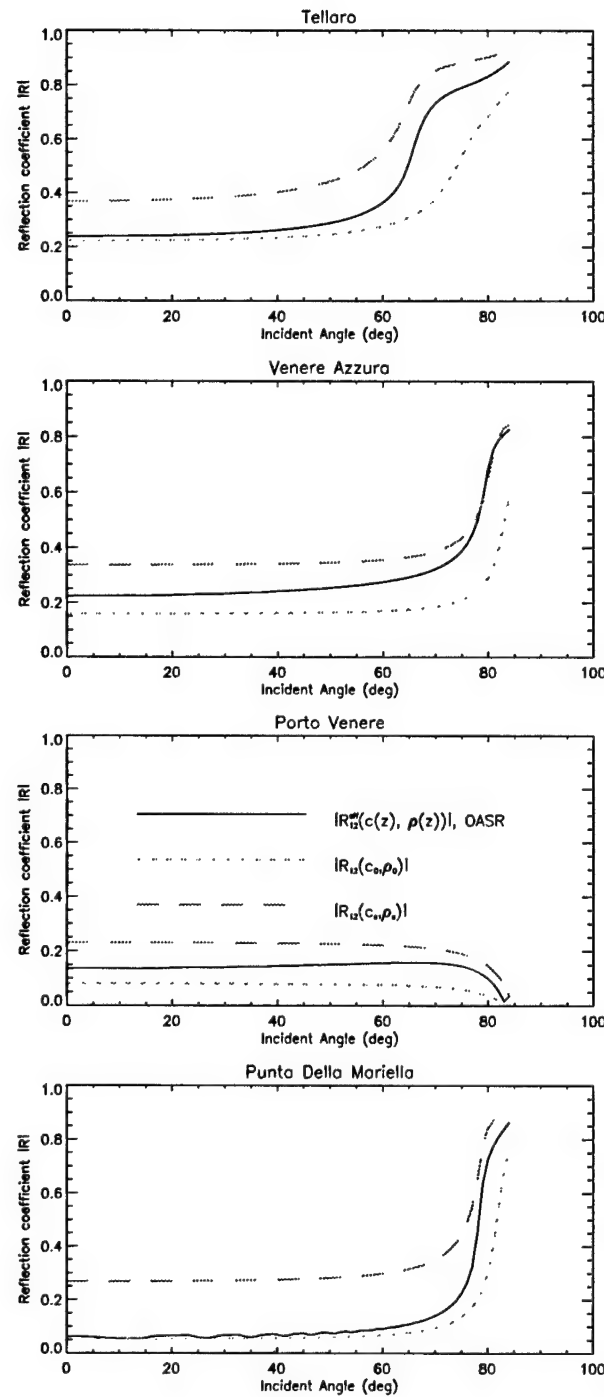


Figure 24 Effect of the vertical gradient on the reflection coefficient. The effective reflection coefficient $R_{12}^{eff}(c(z), \rho(z))$ is computed using OASR.

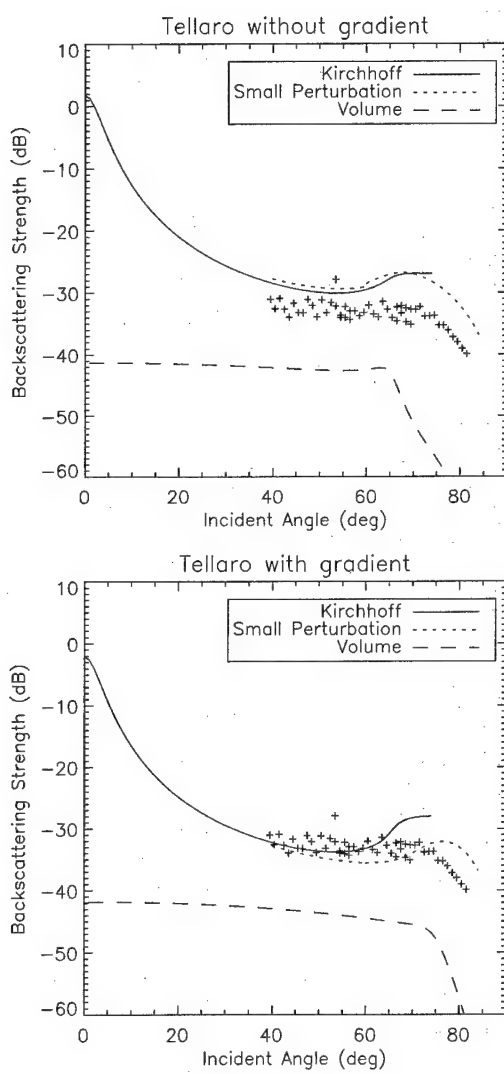


Figure 25 *Model-Data comparison for the Tellaro case.*

BEST AVAILABLE COPY

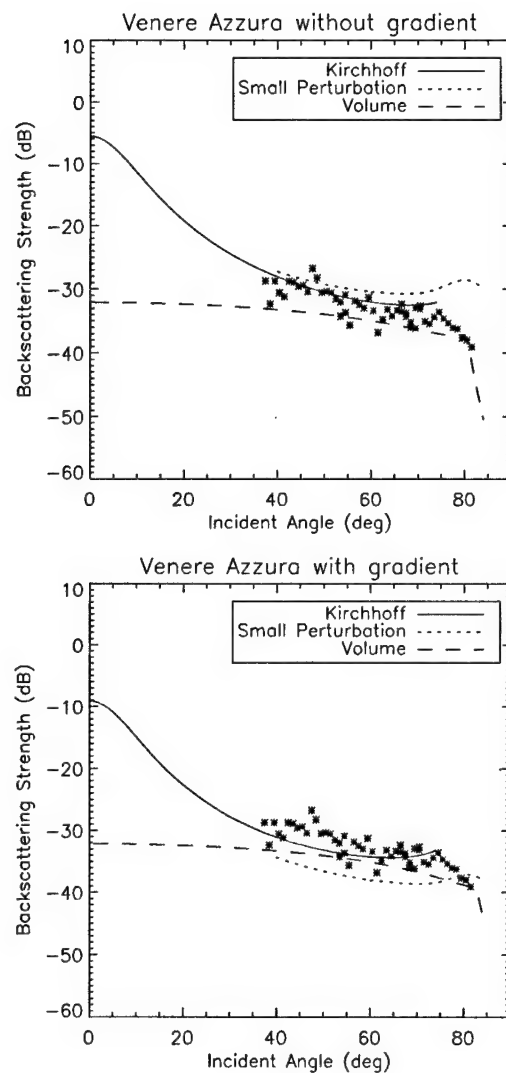


Figure 26 Model-Data comparison for the Venere Azzura case.

BEST AVAILABLE COPY

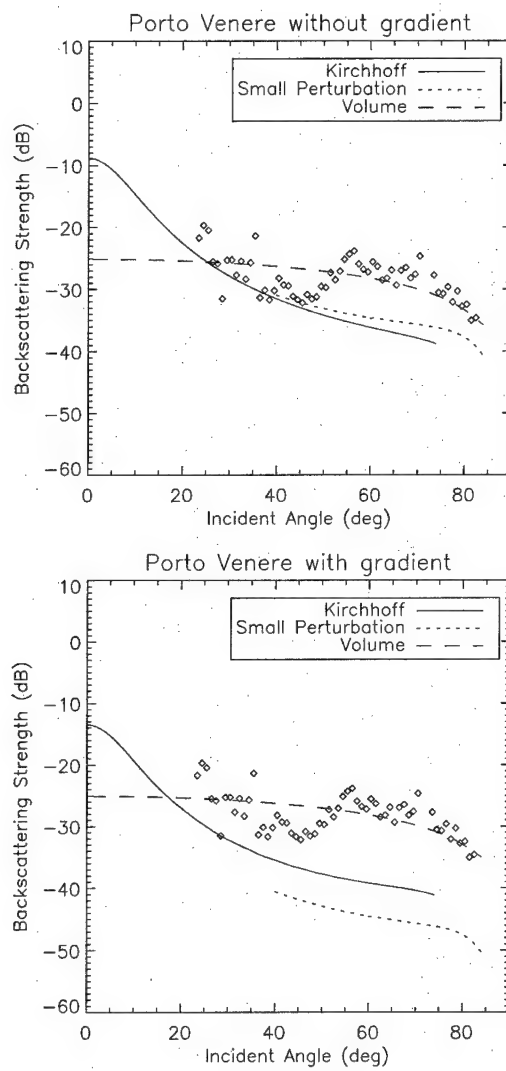


Figure 27 Model-Data comparison for the Porto Venere case.

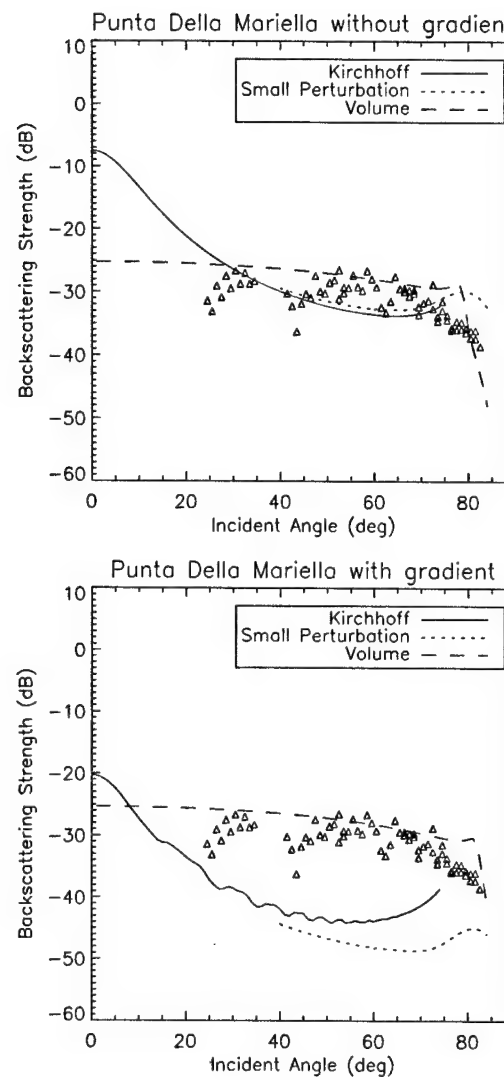


Figure 28 Model-Data comparison for the Punta Della Mariella case.

5

Summary

Four sites in the Gulf of La Spezia (Italy) have been carefully geoacoustically characterized using in particular X-Ray computed tomography on cores and digital photogrammetry on stereo photograph pairs. This thorough characterization has allowed a simple backscattering model to be constrained. A comparison between backscattering data versus angle acquired at four sites comprised of unconsolidated sediments and the developed model has been presented. For two of the sites (PV and PdM), volume backscattering from velocity and density fluctuations explains the high backscattering levels. It also suggests that consideration of gradients in density and sound speed are necessary to explain the measured levels. Regarding the correct way of treating scattering from an inhomogeneous medium bounded by a rough interface and affected by gradients, many questions still remain to be answered. It is also evident that at high frequency, *in situ* geoacoustic measurements of high spatial resolution and accuracy become more delicate and important.

We can conclude with the following comments:

- The density structure of highly bioturbated sediments does not seem to behave like a modified power law in the low spatial frequency portion of the power spectrum. However, at high spatial frequencies (typically above $\log_{10}(k) > 2.8$ which corresponds to acoustic frequencies higher than 75kHz in the backscattering case, the power spectrum decay can be acceptably described by a power-law. At high spatial frequencies, the power exponent of the density structure γ_1 seems to increase as the level of fluctuation increases: (TE: $\gamma_1 = 2.2$, VA: $\gamma_1 = 2.2$, PV: $\gamma_1 = 2.8$, PdM: $\gamma_1 = 3.0$). However, the size and number of the core samples may not be sufficient to draw conclusions on the general behavior of the density power spectrum of bioturbated sediments, especially at the lower frequency end. More and larger core samples are needed to draw general conclusions at lower spatial frequencies.
- At the most bioturbated/heterogenous sites (PV and PdM) and in the moderate to low grazing angle region, the dominance of scattering is essentially caused by a high level of internal geoacoustic property fluctuation.
- In this study, the sediment density structure of highly bioturbated fine sediments is mainly isotropic in the upper 10 cm.

- Vertical gradients have a major effect on backscattering, especially as the acoustic frequency increases. When the acoustic wavelength is of the order or smaller than the vertical size of the gradient, the relative contribution for the rough interface to the total scattering process is significantly reduced. In the absence of gradients, model-data comparisons are not satisfactory. However, when gradients are taken into account, model-data comparisons are greatly improved.
- The simple models presented here, despite the general agreement with the measured backscattering strength may not be accurate in the very low grazing angle region. They do not account for mechanisms such as anisotropy of the interface, interface and volume multiple scattering, the coupling between a rough boundary and an inhomogenous medium, combined density/velocity/attenuation gradient effect, bioturbation, discrete scatters, gradients in the heterogeneity statistics, etc. These aspects warrant particular attention in future research works.
- It should also be stressed that even though current technology (e.g. digital photogrammetry and X-Ray tomography) enables a better statistical description of the geoacoustic environment, this technology may still remain insufficient above 100 kHz given the complexity of the considered seabeds and the scattering mechanisms taking place in them.

Acknowledgments

The authors would like to acknowledge the crew of the Manning (A. Spairani, G. Ciuffardi, G. Bertoli), the SACLANTCEN Engineering and Technology Department (Richard Stoner and E. Michelozzi in particular), Tim Orsi from Planning Systems Inc., Lanfranco Muzzi for help with CT scans, P.A.G. Thompson from UK/Defence Evaluation and Research Agency for the acquisition and processing of the acoustic signals, the divers (M. Paoli and J.R. Staveley) and B. Tonarelli for the grain size analysis.

References

- [1] A.V. Bunchuk & Y.Y. Zhitovskii, *Sound scattering by the ocean bottom in shallow-water regions (review)*, Sov. Phys. Acous. 26(5), 363-370, Sept-Oct 1980.
- [2] Y.Y. Zhitkovskii, Y.P. Lysanov, *Reflexion and scattering of sound from the ocean bottom (Review)* Sov. Phys. Acoust. 30 (5), 1-13, July-September. 1967.
- [3] H.K Wong & W.D. Chesterman, *Bottom backscattering near grazing incidence in shallow water* J. Acous. Soc. Am. 44, 1713-1718, 1968.
- [4] Y.Y. Zhitkovskii, L.A. Volovova , *Sound scattering from the ocean bottom* 5eme Congrès International d'Acoustique, Liège 7-14 Septembre 1965.
- [5] C. M. Mc Kinney & C. D. Anderson, *Measurement of backscattering of sound from the ocean bottom* J. Acous. Soc. Am. 36, 158-163, 1964.
- [6] R.J. Urick, *The backscattering of sound from a harbor bottom* J. Acous. Soc. Am. 26 (2) 231-235, 1954.
- [7] R.J. Urick, *Principles of Underwater Sound* Mc-Graw-Hill, New York, 1983 3rd edition.
- [8] D. R. Jackson, K. B. Briggs, *High-Frequency bottom backscattering: Roughness versus sediment volume scattering*, J. Acoust. Soc. Am., vol.92 (2), pp.962-977, August 1992.
- [9] D. R. Jackson, K. B. Briggs, K. L. Williams, M. D. Richardson, *Test of models for high-frequency seafloor backscatter*, IEEE Journal of Oceanic Engineering, volume 21 (4), pp. 458-470, October 1998.
- [10] S. Stanic, K.B. Briggs, P. Fleisher, W.B. Sawyer & R.I.Ray, *High-Frequency acoustic backscattering from a coarse shell ocean bottom* J. Acous. Soc. Am. 85 (1), 125-136, 1989.
- [11] A.P. Lyons, W.L.J. Fox, T. Hasiotis, E. Pouliquen, *Characterization of the two-dimensional roughness of shallow-water sandy seafloors* submitted to I.E.E.E Journal of Oceanic Engineering.
- [12] T. H. Orsi and A. L. Anderson,, *Bulk density calibration for X-ray tomographic analyses of marine sediments*, Geo-Marine Lett., 19, 270-274 (1999).
- [13] D. Tang, T.H. Orsi, *Three-dimensional density spectra of sandy sediments*, J. Acoust. Soc. Am., 107 (4), pp. 1953-1963, April 2000.

- [14] P. Blondel, B. J. Murton, "Handbook of Sonar Imagery", Wiley-Praxis Series, 1997.
- [15] D. R. Jackson, D. P. Winebrenner, *Application of the composite roughness model to high frequency bottom backscattering*, J. Acoust. Soc. Am., vol.79 (5), pp.1410-1421, May 1986.
- [16] T. Yamamoto, *Acoustic scattering in the ocean from velocity and density fluctuations in the sediments*, J. Acoust. Soc. Am., vol.99 (2), pp.866-879, February 1996.
- [17] L. A. Chernov, *Wave propagation in a random medium*, Mac Graw-Hill, part. 2, 1960.
- [18] M. Bruneau, *Introduction aux théories de l'acoustique* ed. Universit du Maine, 1983.
- [19] A. N. Ivakin, Yu. P. Lysanov, *Underwater sound scattering by volume inhomogeneities of a bottom medium bounded by a rough surface*, Sov. Phys. Acoust., vol.27 (3), pp.212-215, January 1988.
- [20] E. I. Thorsos, *The validity of the Kirchhoff approximation for rough surface scattering using a Gaussian roughness spectrum*, J. Acoust. Soc. Am., vol.83(1), pp.78-92, Jan. 1988.
- [21] E. I. Thorsos, *The validity of the perturbation approximation for rough surface scattering using a Gaussian roughness spectrum*, J. Acoust. Soc. Am., vol. 86 (1), pp.261-277, July 1989.
- [22] E. Y. T. Kuo, *Wave transmission and scattering at irregular interfaces*, J. Acoust. Soc. Am., vol. 36, pp.2135-2142, Nov. 1964.
- [23] T. Yamamoto, *Velocity variability and other physical properties of marine sediments measured by crosswell acoustic tomography*, J. Acoust. Soc. Am., vol.98 (4), pp.2235-2248, October 1995.
- [24] A. Ivakin, , J. Acoust. Soc. Am., volume 96, p 1748, 1994.
- [25] A. P. Lyons, T. H. Orsi, "The effect of layer of varying density on high-frequency reflection, forward loss and backscatter", IEEE Journal of Oceanic Engineering, volume 23 (4), pp. 411-422, October 1998.
- [26] H. Schmidt, *Oases Version 2.2: User Guide and Reference Manual*, Massachusetts Institute of Technology, 1999.
- [27] E. L. Hamilton, *Geoacoustic modeling of the seafloor*, J. Acoust. Soc. Am., volume 68 (5), pp. 78-92, January 1988.

Document Data Sheet

Security Classification UNCLASSIFIED		Project No. 03-D
Document Serial No. SR-342	Date of Issue June 2001	Total Pages 46 pp.
Author(s) Pouliquen, E., Lyons, A.P., Pace, N.G., Michelozzi, E., Muzi, L.		
Title Backscattering from bioturbated sediments at very high frequency.		
Abstract <p>Recent backscattering measurements made in the Gulf of La Spezia (Italy) using a sonar operating at 140 kHz combined with thorough seabed interface and volume ground truth illustrate the dominance of seabed volume scattering. Three-dimensional fluctuation statistics of density variability and vertical density gradients, both of which relate directly to the level of bioturbation (e.g. sea shell fragments, burrows, pockets of water) have been quantified using X-Ray computed tomography. Two-dimensional interface roughness spectra have also been determined using a digital stereo photogrammetry system. The combined ground truth has allowed a backscattering model to be fully constrained. Measured backscattering strength versus angle is compared to a model that includes the effects of varying density and sound speed. Data-model comparisons show that scattering from the volume of strongly inhomogeneous sediments can often be a primary contributor to seafloor scattering away from normal incidence.</p>		
Keywords High-frequency acoustics - acoustic scattering - seafloor scattering		
Issuing Organization North Atlantic Treaty Organization SACLANT Undersea Research Centre Viale San Bartolomeo 400, 19138 La Spezia, Italy <i>[From N. America: SACLANTCEN (New York) APO AE 09613]</i>	Tel: +39 0187 527 361 Fax: +39 0187 527 700 E-mail: library@saclantc.nato.int	

BEST AVAILABLE COPY

The SACLANT Undersea Research Centre provides the Supreme Allied Commander Atlantic (SACLANT) with scientific and technical assistance under the terms of its NATO charter, which entered into force on 1 February 1963. Without prejudice to this main task - and under the policy direction of SACLANT - the Centre also renders scientific and technical assistance to the individual NATO nations.

This document is approved for public release.
Distribution is unlimited

SACLANT Undersea Research Centre
Viale San Bartolomeo 400
19138 San Bartolomeo (SP), Italy

tel: +39 0187 527 (1) or extension
fax: +39 0187 527 700

e-mail: library@sACLANTC.nato.int

NORTH ATLANTIC TREATY ORGANIZATION

BEST AVAILABLE COPY